

Dust storms originating in the northern hemisphere during the third mapping year of Mars Global Surveyor

Huiqun Wang

Atomic and Molecular Physics Division, Smithsonian Astrophysical Observatory, 60 Garden St., Cambridge, MA 02138, USA

Received 28 April 2006; revised 24 December 2006

Available online 24 February 2007

Abstract

Data from the third Mars Global Surveyor (MGS) mapping year (MY 26, 2003–2005) are used to investigate dust storms originating in the northern hemisphere. Flushing dust storms, which originate as frontal dust storms at the northern polar vortex edge and propagate southward through topographic channels, are observed immediately before and after a quiescent period that occurs around the northern winter solstice ($240^\circ < L_S < 300^\circ$). Both the pre- and post-solstice active periods can be further divided into two sub-periods. The most vigorous of these flushing storms occurred during L_S 210–220° and L_S 310–320°. The lifted dust crossed the equator and accumulated in the southern hemisphere. These major dust storms enhanced the Hadley circulation and suppressed the lower-level baroclinic eddies in the northern mid and high latitudes. The 2–3 sol wave number $m = 3$ traveling waves show the best correlation with flushing dust storms and can combine with other wave modes to produce storm tracks and fronts within individual sub-periods.

© 2007 Elsevier Inc. All rights reserved.

Keywords: Mars, atmosphere

1. Introduction

Mars Global Surveyor (MGS) has been continuously monitoring global martian meteorology for more than three Mars years. The data returned by MGS have been used to study the distribution of dust, clouds, and water vapor in great detail (e.g., Cantor et al., 2001; Wang and Ingersoll, 2002; Smith, 2004; Wang et al., 2005). Among the many findings of MGS are the “flushing dust storms” which originate at the north polar vortex edge as frontal dust storms and propagate southward through confined longitude channels (Cantor et al., 2001; Wang et al., 2003). The most intense flushing storms can transport dust across the equator to the southern hemisphere. Flushing events initially keep the curved or linear frontal structures indicative of baroclinic eddies; however, once the dust storms move south, they usually exhibit irregular patchy shapes and can be enhanced by additional dust lifting along the way. Using the data obtained by MGS from 1999 to 2003, Wang et al. (2005) showed that flushing dust storms are concentrated

in Acidalia, Arcadia, and Utopia, are active during the periods away from the northern winter solstice, and correlate especially well with the 2–3 sol wavenumber $m = 3$ eastward traveling waves in the lowest atmospheric scale height. Furthermore, Wang et al. (2003) suggested that consecutive flushing dust storms could lead to major dust storms of global impact.

The development of flushing storms involves interactions among baroclinic eddies, thermal tides, and the Hadley circulation (Wang et al., 2003). Together with the suggestion that major dust storms could suppress subsequent development of baroclinic eddies (Leovy et al., 1985; Wang et al., 2005), this led Wang et al. (2005) to hypothesize that the timing of major dust storms could affect the seasonal distribution of flushing dust storms: a major dust storm in the early fall or mid winter could be followed first by a period with no frontal dust storms, and, subsequently, by a period with active flushing dust storms. An overview of past work can be found in Wang et al. (2005), and is not repeated here.

To investigate the interannual variability and test the hypothesis in Wang et al. (2005), this paper presents the distribution of dust storms originating in the northern hemisphere during the third MGS mapping year (MY 26, 2003–2005). The dust storms

E-mail address: hwang@cfa.harvard.edu.

are either flushing dust storms or are related to flushing dust storms. The histories of two dust storm sequences initiated by flushing dust storms are described in detail. These dust storms propagated from the northern to the southern hemisphere and resulted in dust accumulation in the southern hemisphere. The impacts of these dust storms on the atmospheric thermal structures and transient eddy activities are also investigated.

2. Data

This study mainly uses the Mars Daily Global Maps (MDGM) derived from the MGS Mars Observer Camera (MOC) global map swaths and the vertical temperature profiles and dust opacities derived from the MGS Thermal Emission Spectrometer (TES) spectra. MDGM are composed using the method described in Wang and Ingersoll (2002), and are analyzed using the same method as that in Wang et al. (2005). Version 2 MGS TES temperatures and opacities are extracted using the “vanilla” software from the released archives at the Planetary Data System (PDS). The TES data selection criteria include “atm_pt_rating = 0, atm_opacity_rating = 0 (the retrieval is good), and emission angle <5°”. Some MGS MOC wide angle images and MGS Radio Science temperature profiles are presented as supplementary materials in this paper as well.

3. Dust storm distribution

3.1. MOC observations

Fig. 1 shows the L_s -latitude distribution of dust storms that occur within 60° S–60° N, originate in the northern hemisphere, and show history or morphology indicative of southward motion. The method for selecting dust storms is the same as that in Wang et al. (2005). Figs. 1a and 1b show the updated version for the first (MY 24, 1999–2001) and second (MY 25, 2001–2003) MGS mapping years, and Fig. 1c shows the newly completed results for the third (MY 26, 2003–2005) MGS mapping year. All flushing dust storms (Wang et al., 2003, 2005) are tracked: diamonds with plus signs indicate new flushing dust storms, hollow diamonds indicate both dust storms that result from flushing dust storms and a few ambiguous dust storms. Dust storms that last multiple days or dust storms that merge are connected with lines. There are 142, 108, and 162 new flushing dust storms in Figs. 1a, 1b, and 1c, respectively. Fig. 1 does not include dust storms that are clearly associated with topography or albedo, or dust storms that originate in the southern hemisphere. However, with the exception of the 2001 (MY 25, $L_s \sim 182^\circ$) global dust storm which shows explosive development from the southern to the northern hemisphere (Smith, 2004; Strausberg et al., 2005), Fig. 1 provides a good summary of the main dust storm activities within 60° S–60° N.

A detailed study of the first and second MGS mapping years (MY 24 and MY 25) can be found in Wang et al. (2005), this paper concentrates on the third year (MY 26). In agreement with the previous two years, flushing dust storms in MY 26 are confined to two separate seasonal windows: the pre-solstice and

post-solstice periods. During the “gap” period (L_s 240°–300°) between the two seasonal windows, streaks are present at the edge of the north polar hood and the atmosphere appears dusty, but no frontal dust storms are observed. Detailed examination of Fig. 1c shows that within each seasonal window, there are two active sub-periods of flushing dust storms with a short gap between them. Although each active sub-period contains only a few flushing dust storms, they both include one long-lasting (more than \sim one week) dust storm sequence. The pre-solstice window contains the short gap of $L_s \sim 220^\circ$ – 230° and the post-solstice window contains the short gap of $L_s \sim 320^\circ$ – 330° . There are 8, 3, 10, and 12 distinct flushing events during L_s 210°–220°, L_s 230°–240°, L_s 310°–320°, and L_s 330°–340°, respectively. Short gaps are not apparent in MY 24 and MY 25 (Figs. 1a and 1b). Later sections will show that the flushing dust storms before $L_s \sim 220^\circ$ and those before $L_s \sim 320^\circ$ have a significant impact on the global atmospheric temperature structures during the short gaps, and that the effects of the perturbations subside before the next active flushing sub-period begins. The flushing dust storms in the post-solstice periods of MY 24 and MY 25 did not have appreciable effects on the large-scale temperature structures, which might be the reason for the lack of short gaps during these periods. Although the flushing storms in the pre-solstice period of MY 24 led to the 1999 planet-encircling dust storm which significantly perturbed the atmospheric temperatures (Liu et al., 2003; Smith (2004); Wang et al., 2003, 2005), the long northern winter solstice gap had begun by the end of this storm ($L_s \sim 240^\circ$), preventing a second period of flushing dust storms before the solstice. Had the 1999 planet-encircling storm finished earlier, there could have been an additional episode of flushing dust storms in the northern fall of MY 24.

Fig. 2 shows representative equatorial MDGM (60° S–60° N, 180° W–180° E) for the sequence of dust storms before $L_s \sim 220^\circ$ of MY 26. Active frontal dust storms have been traveling eastward around the northern polar cap since late northern summer. As the season progresses, the latitude zone with active frontal dust storms extends southward and intersects the topography at lower latitudes. The frontal dust storms also tend to grow in size with time, penetrating to lower latitudes in the low-topography regions of Acidalia, Arcadia, and Utopia Planitias, where they form large flushing dust storms. In the early fall of MY 26, Utopia Planitia hosts the most vigorous flushing storms of the season. The L_s 210°–220° cross-equatorial dust storm sequence is preceded by flushing dust storms that occur on a daily basis (e.g., Fig. 2a). Fig. 2b shows the beginning frame of the L_s 210°–220° dust storm sequence. This sequence is tracked in MDGM for the next two weeks or so (Figs. 2b–2h). The storms in Fig. 2b start as small frontal dust storms which grow in size as they move southward toward the boundary between Isidis Planitia and Tyrrhena Terra (Fig. 2c). The curved dust band structure is lost when dust propagates southward across this albedo and topographic boundary, and the storms subsequently appear amorphous and diffuse (Figs. 2d–2h). After dust arrives at the region to the northeast of Hellas, it appears to be enhanced by dust lifted in the vicinity of Hellas. The main propagation direction changes first to a westward, and then to

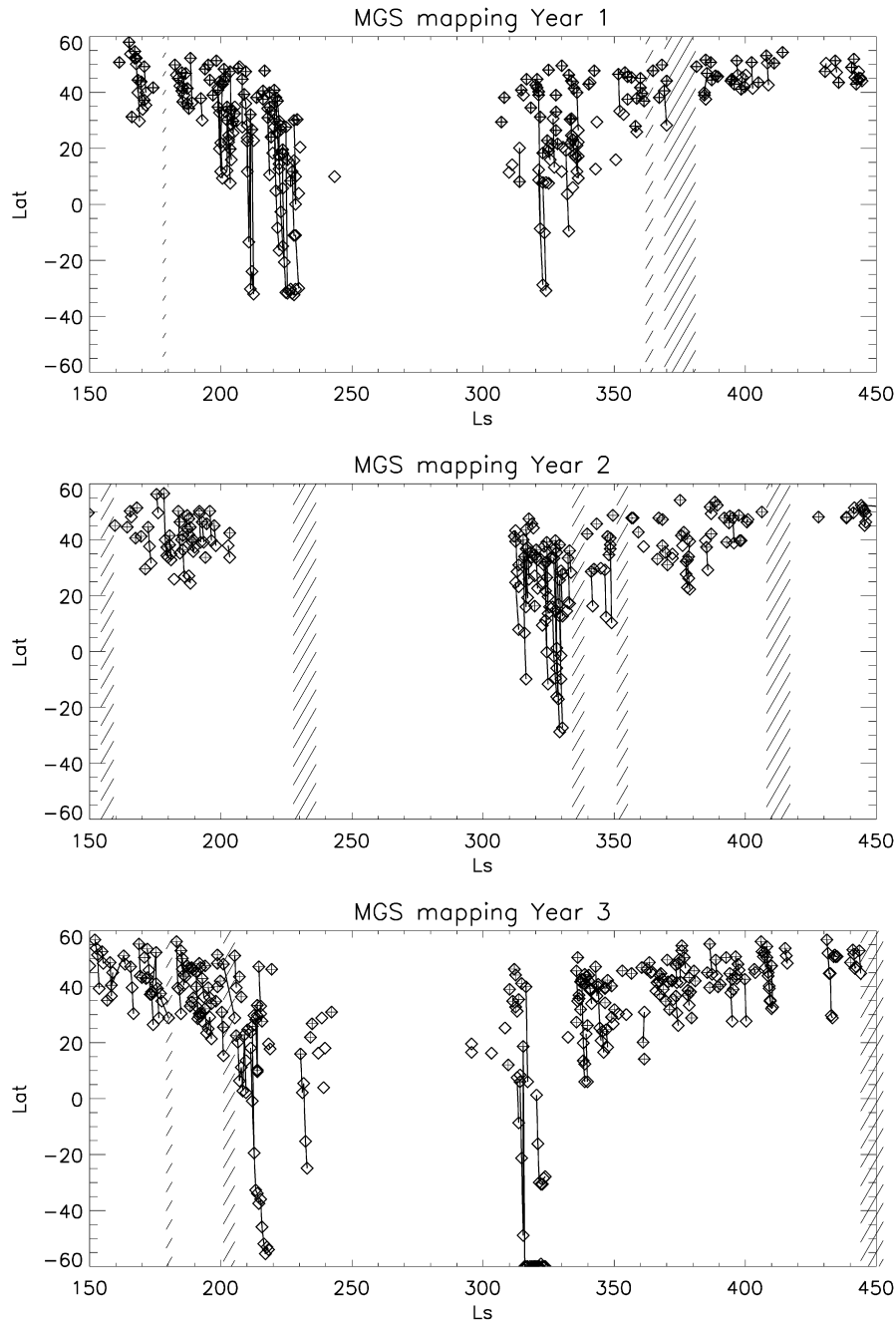


Fig. 1. L_s –latitude distribution of dust storms originating in the northern hemisphere. The three panels show results for MGS mapping years 1 (MY 24, 1999–2001), 2 (MY 25, 2001–2003), and 3 (MY 26, 2003–2005), respectively. Diamonds with plus signs indicate new frontal dust storms (frontal dust storms suggestive of southward motion). Hollow diamonds are either dust storms that can be traced to previous storms or questionable flushing dust storms. Dust storms that last multiple days or dust storms that merge are connected with lines. The regions in shadows indicate periods with no images.

a southward direction (Figs. 2e–2h). Dust temporarily accumulates in Noachis Terra (west of Hellas, Fig. 2h) and dissipates within about four days. During the course of this sequence, several flushing dust storms are observed in Acidalia and Arcadia (e.g., Fig. 2f), although these storms do not cross the equator. After the sequence finishes at $L_s \sim 219^\circ$, there is a ~ 20 -day hiatus when the northern mid and high latitudes are dominated by streaks without any flushing dust storms. The hiatus is followed by a brief period (\sim one week, L_s 230° – 235°) of active flushing dust storms in the Acidalia channel. The first flushing

dust storm for this sub-period can be found in Fig. 5i of Wang et al. (2005). It travels southward across the equator and dissipates in the region to the southeast of Valles Marineris’ EOS Chasma.

The post-solstice period starts around $L_s \sim 310^\circ$ when vigorous frontal dust storms return at northern mid and high latitudes. Fig. 3 shows representative MDGM for the sequence of dust storms that can be tracked to the southern hemisphere. The first day (Fig. 3a, $L_s \sim 314^\circ$) of the sequence is preceded by about a week of frontal dust storms, some of which are

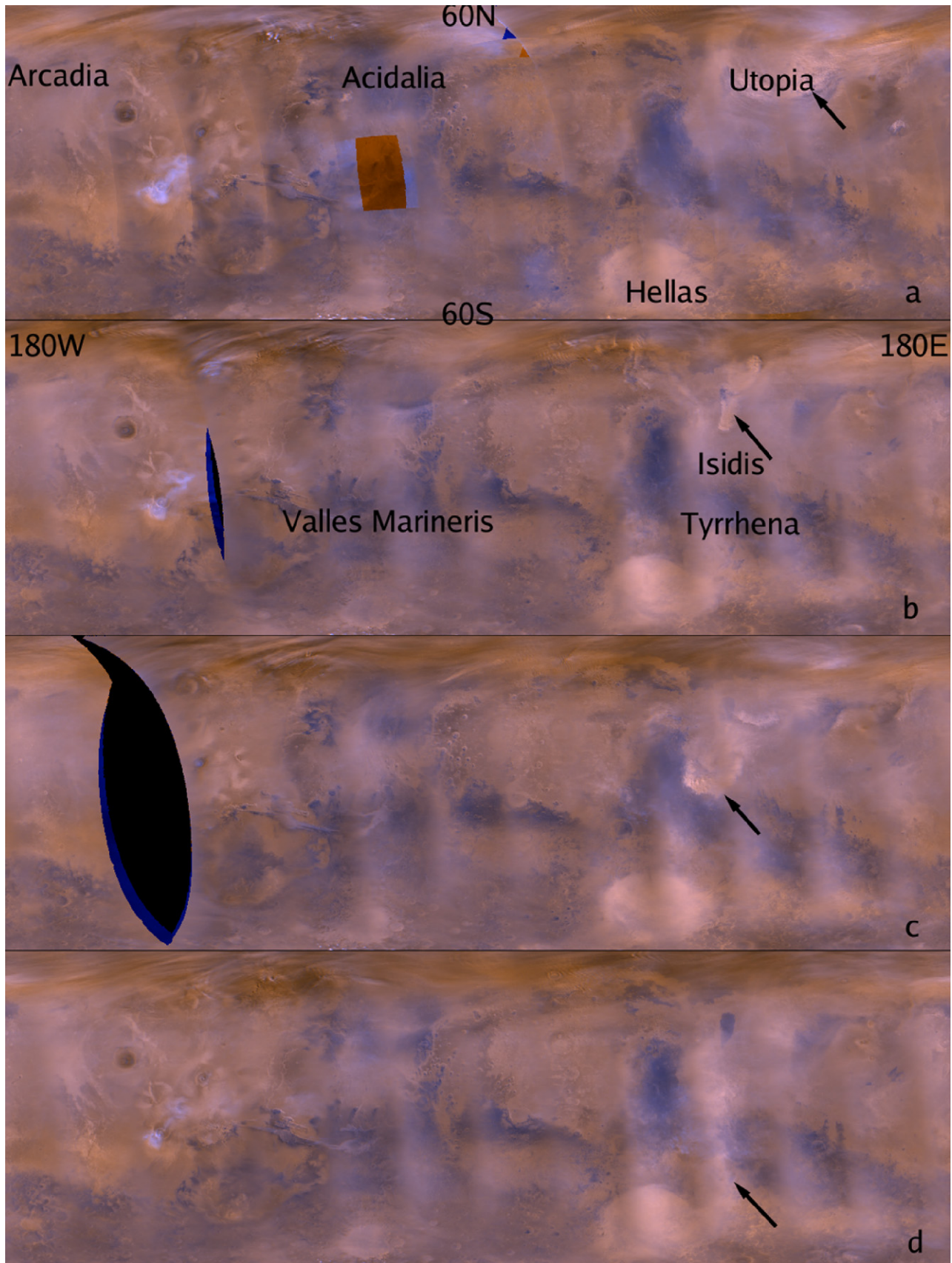


Fig. 2. Representative MDGM (60° S– 60° N, 180° W– 180° E, simple cylindrical projection) illustrating the development of the L_s 210° – 220° dust storm sequence. The L_s for each panel is (a) 206.5° , (b) 211.4° , (c) 212.0° , (d) 212.7° , (e) 213.3° , (f) 213.9° , (g) 214.5° , (h) 215.7° . The dust storms described in the text are indicated by arrows.

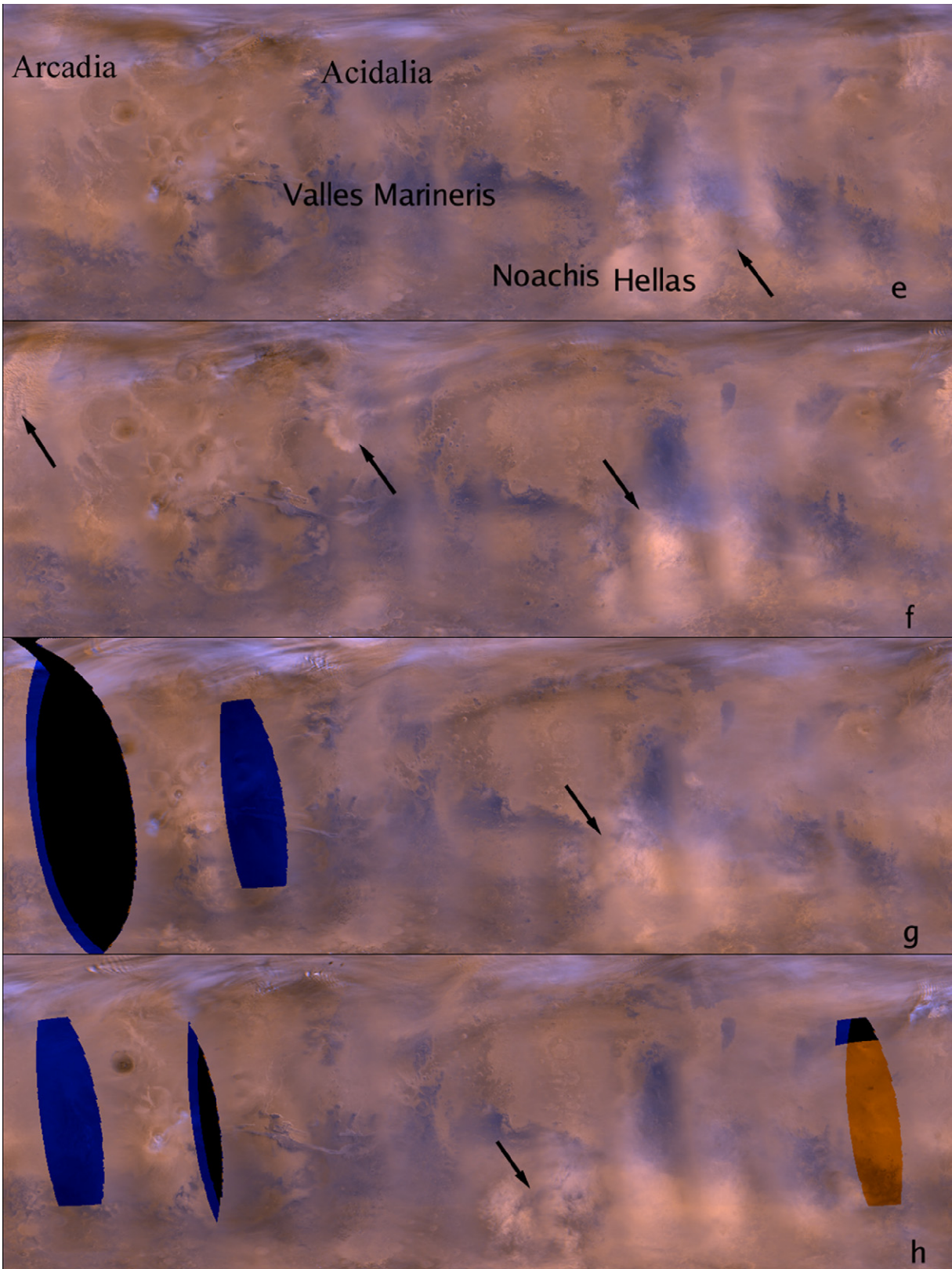


Fig. 2. (continued)

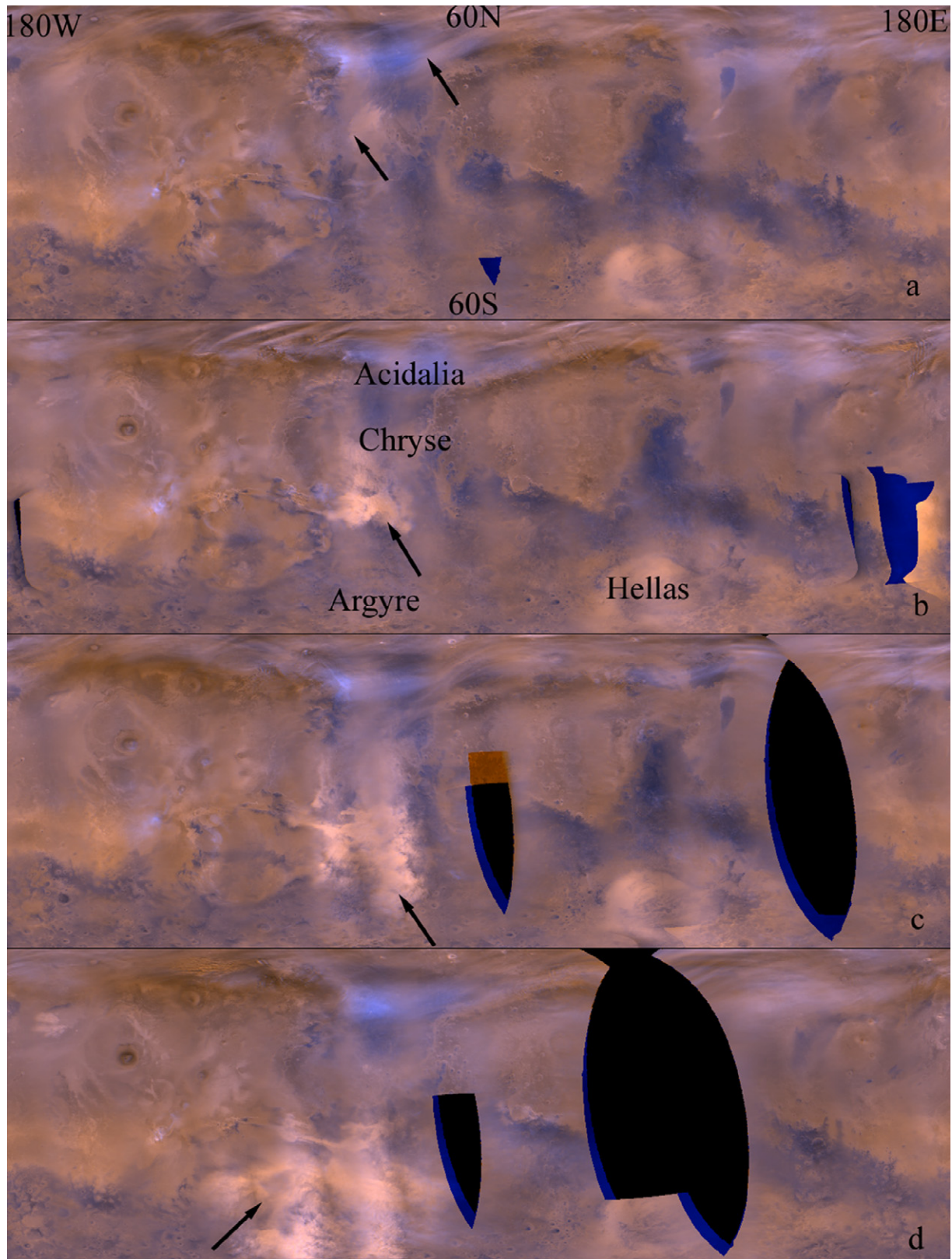


Fig. 3. Representative MDGM (60° S– 60° N, 180° W– 180° E, simple cylindrical projection) illustrating the development of the L_s 310° – 320° dust storm sequence. The L_s for each panel is (a) 314.1° , (b) 314.7° , (c) 315.3° , (d) 315.9° , (e) 316.4° , (f) 317.0° , (g) 319.8° , (h) 320.4° , (i) 320.9° , (j) 321.4° , (k) 322.1° , (l) 322.6° . The dust storms described in the text are indicated by arrows. The rectangles in (i) and (j) indicate the regions displayed in Fig. 4.

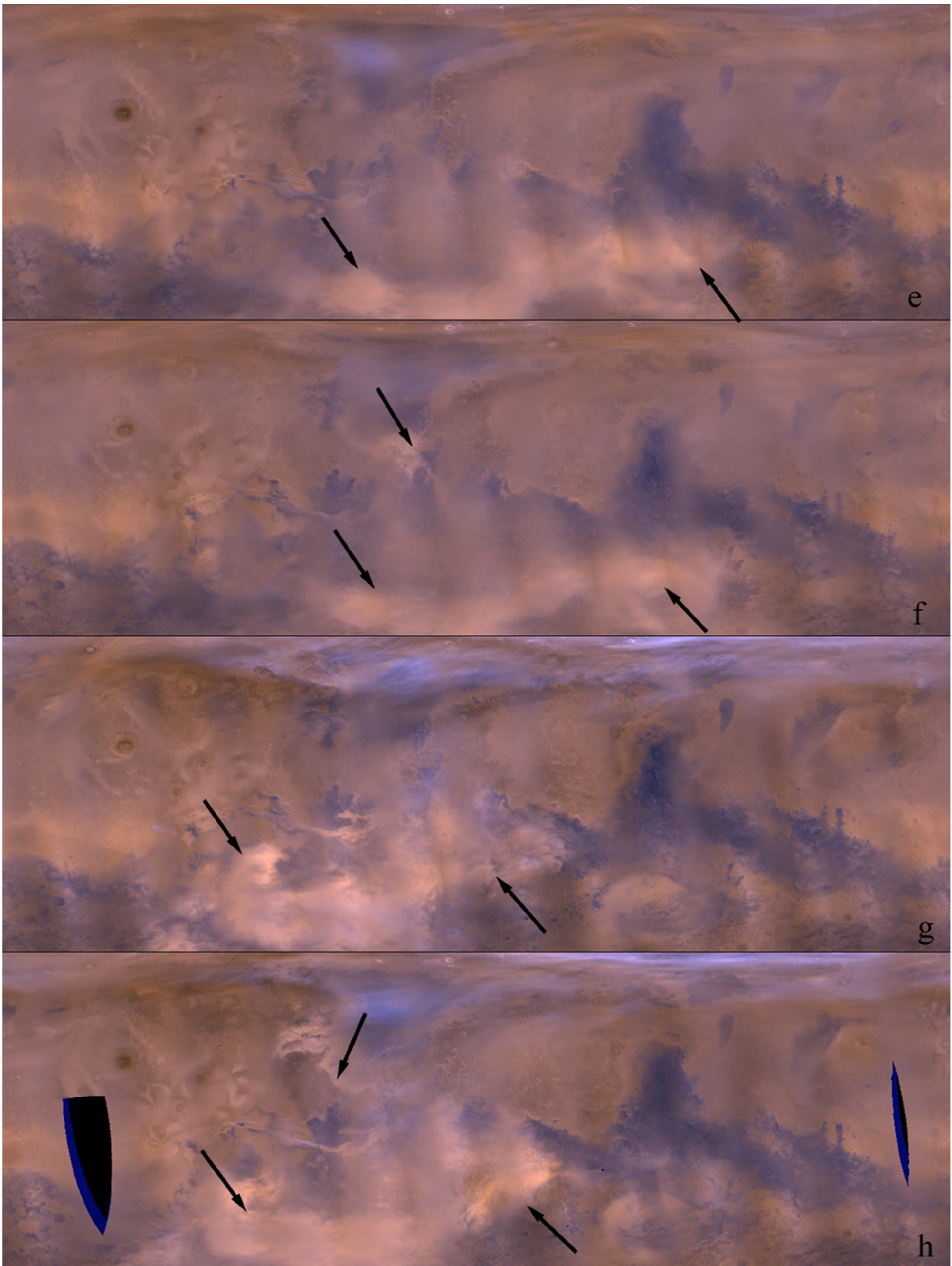


Fig. 3. (continued)

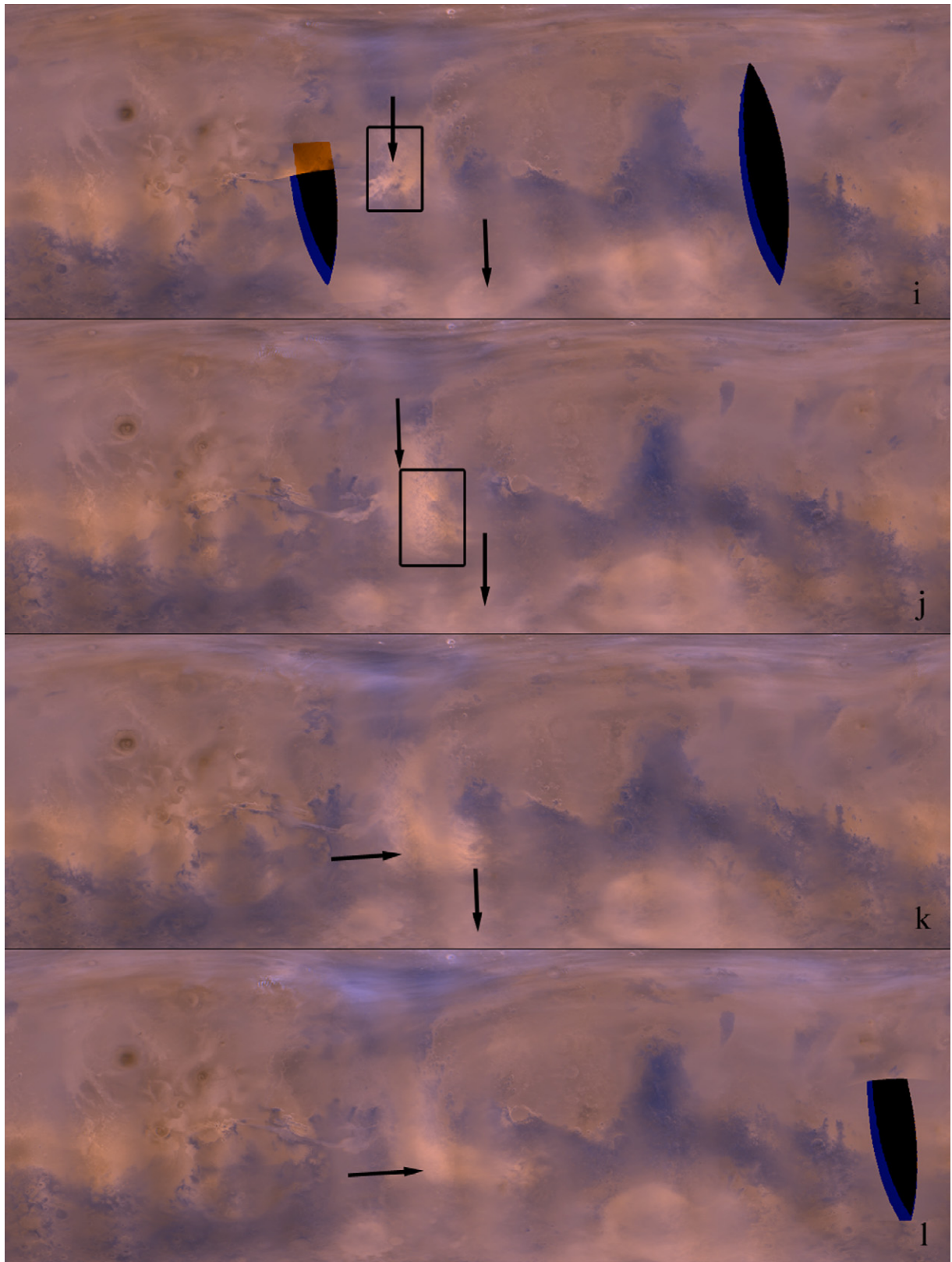


Fig. 3. (continued)

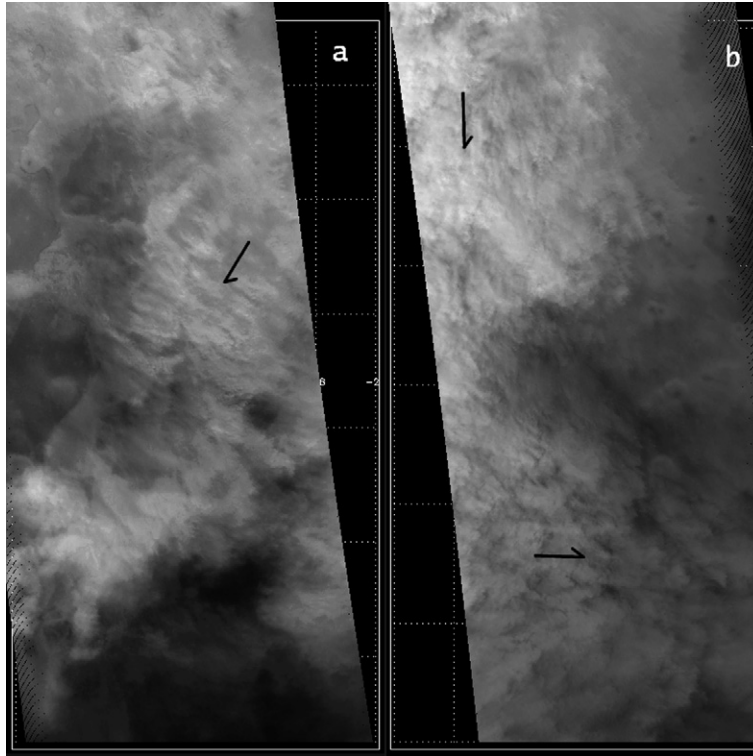


Fig. 4. MGS MOC wide angle image (a) r1202744, $L_s = 321.06$, 1046.45 m/pixel and (b) r1202883, $L_s = 321.61$, 1036.17 m/pixel. The storm in (a) is the same as that near Valles Marineris in Fig. 3i, and the storm in (b) is the same as that near Valles Marineris in Fig. 3j. Both images are in the same simple cylindrical projection as the MDGM. The area in (a) covers 15° S– 10° N, 322° E– 334° E. The area in (b) covers 24° S– 0° , 338° E– 350° E.

flushing dust storms (frontal dust storms that show southward motion). On the first day (Fig. 3a), a flushing dust storm extends its dust band from the polar hood to southern Acidalia Planitia and another dust storm, which may be either dust flushed southward by a previous flushing storm or a local storm, covers Chryse. Dust subsequently travels in a general southward direction for the next three days and reaches latitudes south of 60° S (Figs. 3b–3d), where it appears to be enhanced by dust lifting near Argyre and develops both to the west and to the east (Fig. 3e). Additional flushing dust storms in Acidalia–Chryse also make contributions to the dust load in the southern hemisphere (Fig. 3f). The main body of dust arranges into a southeast–northwest elongated belt that straddles Argyre and Hellas (Figs. 3g–3i). The dust belt gradually merges into the background afterwards (Figs. 3j–3l). In the meantime, some dust from south of Argyre goes to the polar region ($L_s \sim 317^\circ$), and encircles the south polar cap from the west to the east (not shown). The polar dust from this event settles down after about a week. Of all the major dust storms observed by MGS, only the 2001 global dust storm (Strausberg et al., 2005) and this MY 26 L_s 310° – 320° event exported dust to the south polar region. These two major dust storms also have the first and second longest duration of dusty atmosphere in the southern hemisphere. Previous data and numerical simulations show that the presence of substantial amounts of dust in the southern hemisphere during southern spring and summer will significantly affect the global atmospheric structure and circulation (Smith, 2004; Wilson, 1997; Wilson and Richardson, 2000). The im-

pacts of the MY 26 post-solstice dust storms will be presented in later sections.

After the dust belt forms in the southern mid and high latitudes, a second sequence of southward-moving dust storms forms near Chryse at $L_s \sim 320^\circ$ (Fig. 3h). Whether the first storm of this second sequence is related to a flushing dust storm is questionable. Nevertheless, dust travels southward across the equator and temporarily accumulates (for about a week) in the region to the south and east of Valles Marineris (Figs. 3i–3l). This sequence greatly boosts the amount of dust in the southern hemisphere while dust from the previous sequence is dissipating. The MOC WA camera captured 1 km/pixel views of the storms (Fig. 4) in addition to the 7.5 km/pixel global map swaths. Figs. 4a and 4b show the same dust storms as those near Valles Marineris in Figs. 3i and 3j, respectively. A stripe pattern in the northwest–southeast direction is observed in the middle part (just north of Valles Marineris) of Fig. 4a. The direction of the stripes appears to be perpendicular to the direction of dust storm motion (indicated by the arrow). The part south of the stripes appears amorphous, perhaps due to the interaction with the complex terrain of Valles Marineris. The dust storm in Fig. 4b exhibits a fluffy, blotchy texture common to mature dust storms. It has mostly passed Valles Marineris and is traveling in a general southward direction in Margaritifer Sinus (the upper part) and in an eastward direction south of it (the lower part). Curved dark lines or lobes perpendicular to the propagation directions (indicated by the arrows) are discernible in places despite the generally turbulent appearance of the dust storm.

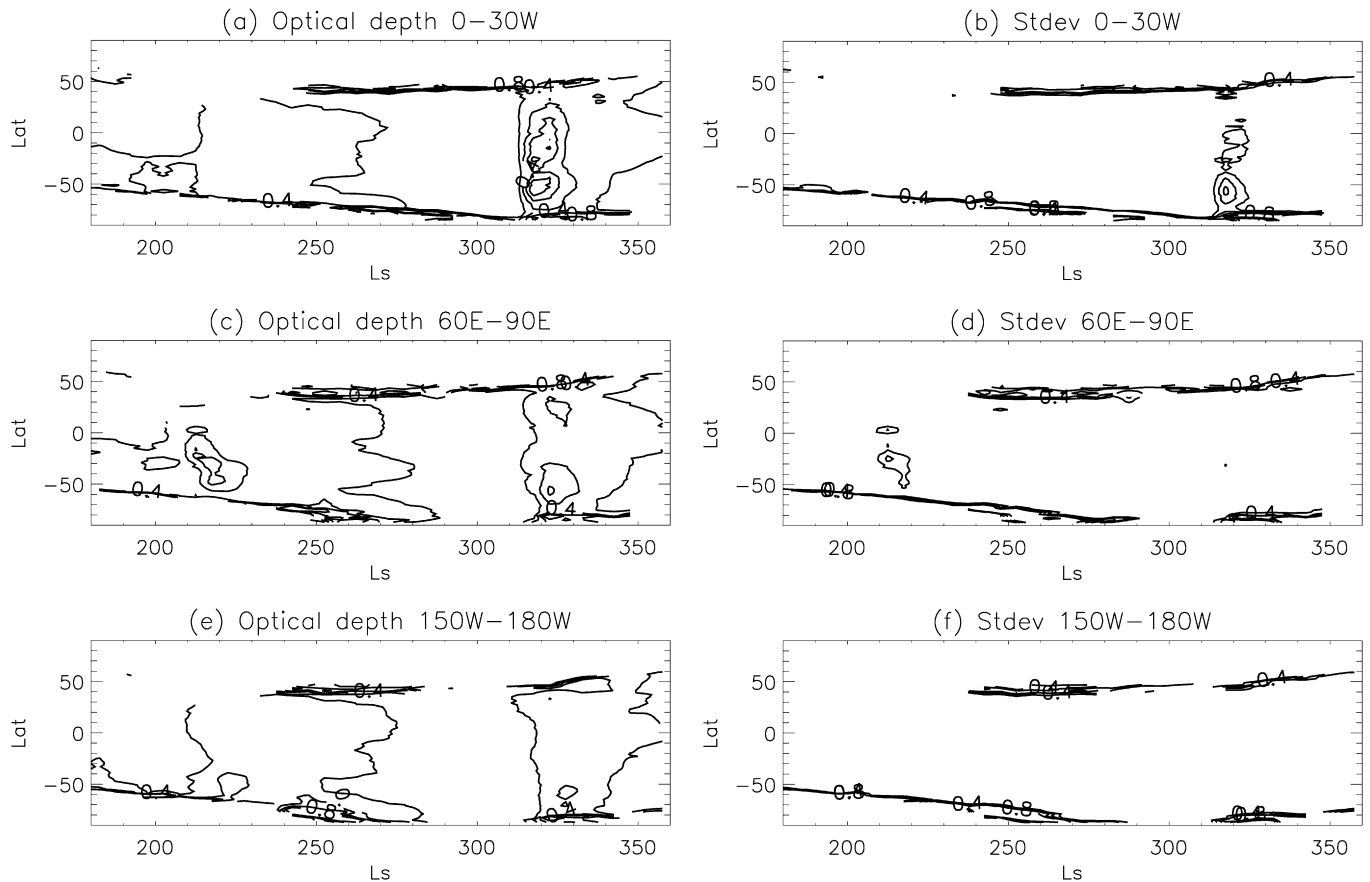


Fig. 5. TES dust optical depths normalized to 6.1 mb in MY 26 for selected longitude sectors (a) 0° – 30° W, (c) 60° E– 90° E, (e) 150° W– 180° W. The standard deviations of normalized dust optical depths for selected longitude sectors (b) 0° – 30° W, (d) 60° E– 90° E, (f) 150° W– 180° W.

With the dissipation of the sequence, the atmosphere acquires a dusty background, but not much dust-storm activity is observed for the next three weeks ($L_s \sim 323^{\circ}$ – 335°). During this ‘quiet’ period, the atmospheric temperature structures and eddies experience dramatic changes (see later sections) which may be responsible for the absence of frontal dust storms during the hiatus. This is somewhat similar to what happened after the 1977b ($L_s \sim 268^{\circ}$) global dust storm (Barnes, 1980). Flushing dust storms return after the $L_s \sim 323^{\circ}$ – 335° hiatus in MY 26, but these later flushing storms are isolated in time and do not produce dust accumulation in the southern hemisphere.

3.2. TES observations

TES provides observations simultaneous with those of MOC. Although TES observations are relatively limited in monitoring day-to-day variations due to the small field of view and large longitudinal separation ($\sim 30^{\circ}$) between adjacent orbits, they are excellent for displaying the large-scale dust distribution and atmospheric temperature evolution. Fig. 5 shows the L_s –latitude distribution of TES dust opacities (scaled to 6.1 mb) and their standard deviations for selected longitude sectors. The standard deviations are calculated for data that lie within 30° longitude by 2° latitude by 5° L_s bins. The scaled dust opacities indicate the dust loading and the standard deviations indicate where transient activity (origination, travel,

dissipation, etc.) occurs. Large values of both quantities suggest active wave activity involving dust. Large opacity and small standard deviation suggest a uniform dust load in the bin.

The TES data confirm the longitudinal distribution of flushing dust storms seen in the MOC observations. Figs. 5a and 5b show the results for the 0° – 30° W longitude sector. Two main dusty periods ($L_s \sim 210^{\circ}$ – 240° and $L_s \sim 310^{\circ}$ – 340°) are present, although only the second period shows large standard deviations. This is consistent with the MOC observations that the Acidalia–Chryse channel is the main channel for the development of the post-solstice flushing dust storms. Small gaps within the dusty periods are not discernable here because of the large bin size used. Figs. 5c and 5d show the results for the 60° E– 90° E longitude sector. Compared to the 0° – 30° W sector shown in Fig. 5a, dust opacities for the pre-solstice period are larger and those for the post-solstice period are smaller. Moreover, only the pre-solstice period shows relatively large standard deviations (Fig. 5d). These results agree well with Utopia–Isidis being the primary flushing dust storm channel for the pre-solstice period in MY 26. Figs. 5e and 5f show the results for the 150° W– 180° W sector. The two dusty periods can still be seen in Fig. 5e, though the opacities are apparently smaller than those in Figs. 5a–5c. No large standard deviations are present between 60° S and 60° N in Fig. 5f, consistent with the absence of significant dust storms in the Arcadia–Amozonis channel this year. The increased dust opacities in this sector are

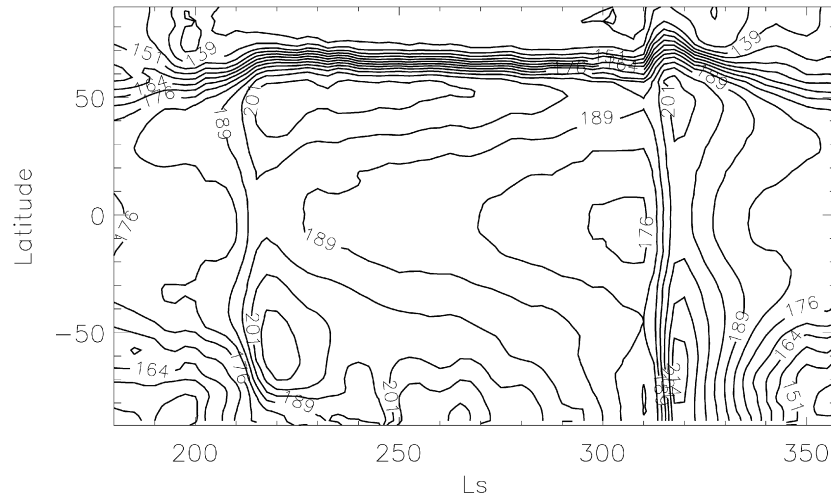


Fig. 6. Zonal mean TES atmospheric temperatures at 50.1 Pa (~ 25 km) as a function of latitude and L_s for MY 26.

mainly attained through atmospheric transport, which is difficult for MDGM to show because the transported dust does not have a clear structure or a boundary. All other longitude sectors also exhibit elevated dust opacities during the two dusty periods, indicating that the dust associated with the pre- and post-solstice dust storms encircled the planet, although the average dust opacities are much smaller than those for global dust storms.

4. Effects on the atmosphere

4.1. The zonal mean temperature

The pre-solstice and post-solstice dusty periods in MY 26 produce a significant impact on global atmospheric temperatures. Fig. 6 shows the zonal-mean temperatures at 0.5 mb (~ 25 km) as a function of latitude and L_s . The rapid increase of temperatures coincides with the initiation of the L_s 210° – 220° and L_s 310° – 320° dust storm sequences. Furthermore, the dusty periods are characterized by dumbbell structures where temperatures at the northern and southern mid latitudes are higher than those at the low latitudes. A dumbbell structure in the upper level temperature field is also associated with the 1999 planet-encircling dust storm and the 2001 global dust storm (Smith et al., 2002; Smith, 2004), and is a signature of an enhanced Hadley circulation associated with major dust storms (Haberle et al., 1993; Wilson, 1997). The perturbation of the L_s 310° – 320° dust storms is especially impressive considering that the isotherms delineating the edge of northern polar vortex protrude to the pole. The only other polar warming in the north polar region was during the solstitial global dust storm observed by Viking (the 1977b storm) (Jakosky and Martin, 1987). No polar warming was associated with the 2001 global dust storm. A simulation of the 1977b global dust storm shows that the polar warming is largely due to the development of a pole-to-pole Hadley circulation, with contribution from the thermal tides (Wilson, 1997). Polar warming does not occur in all global dust storms, but can occur in non-global dust storms which involve

much less dust indicating that the response of the atmospheric circulation depends sensitively on factors other than the dust load, such as the time and mode of dust storm onset.

For all three MGS mapping years, the low-level temperatures in the southern mid and high latitudes reach a maximum around the southern summer solstice (not shown) (Smith, 2004). There is an indication that higher temperatures related to the dust storm sequences occur in the southern hemisphere, but the signal is not as prominent as that in the upper levels. Furthermore, there is no apparent evidence of low-level temperature perturbations in the northern polar region. It therefore appears that the upper level atmospheric temperatures are better indicators of major dust storms than the lower level temperatures.

4.2. Eddies

4.2.1. Standard deviations of temperatures

Wang et al. (2005) showed that lower level temperature perturbations were closely related to flushing dust storms in MY 24 and MY 25. Figs. 7a and 7b show the standard deviations of temperature perturbations for MY 26 at 4.75 mb (~ 2.5 km) derived from the TES 2PM and 2AM temperatures, respectively. The standard deviations are calculated for 30° longitude by 2° latitude by 10° L_s bins and then zonally averaged. The most important contributions to the standard deviations are from the transient eddies. In the southern hemisphere, the maximum during L_s 310° – 320° clearly corresponds to the post-solstice dust storm sequence described in Section 3 and is present in both the 2PM and 2AM plots. There appear to be enhanced 2PM temperature variations in the southern hemisphere during L_s 210° – 220° which would correspond to the pre-solstice cross-equatorial dust storms. However, these enhanced variations are not present in the 2AM plot; Fig. 7 shows that the 2PM variations are generally larger than the 2AM variations. This perhaps relates to the mechanisms preferentially at work during the daytime such as convection and dust devils. Considering that the L_s 210° – 220°

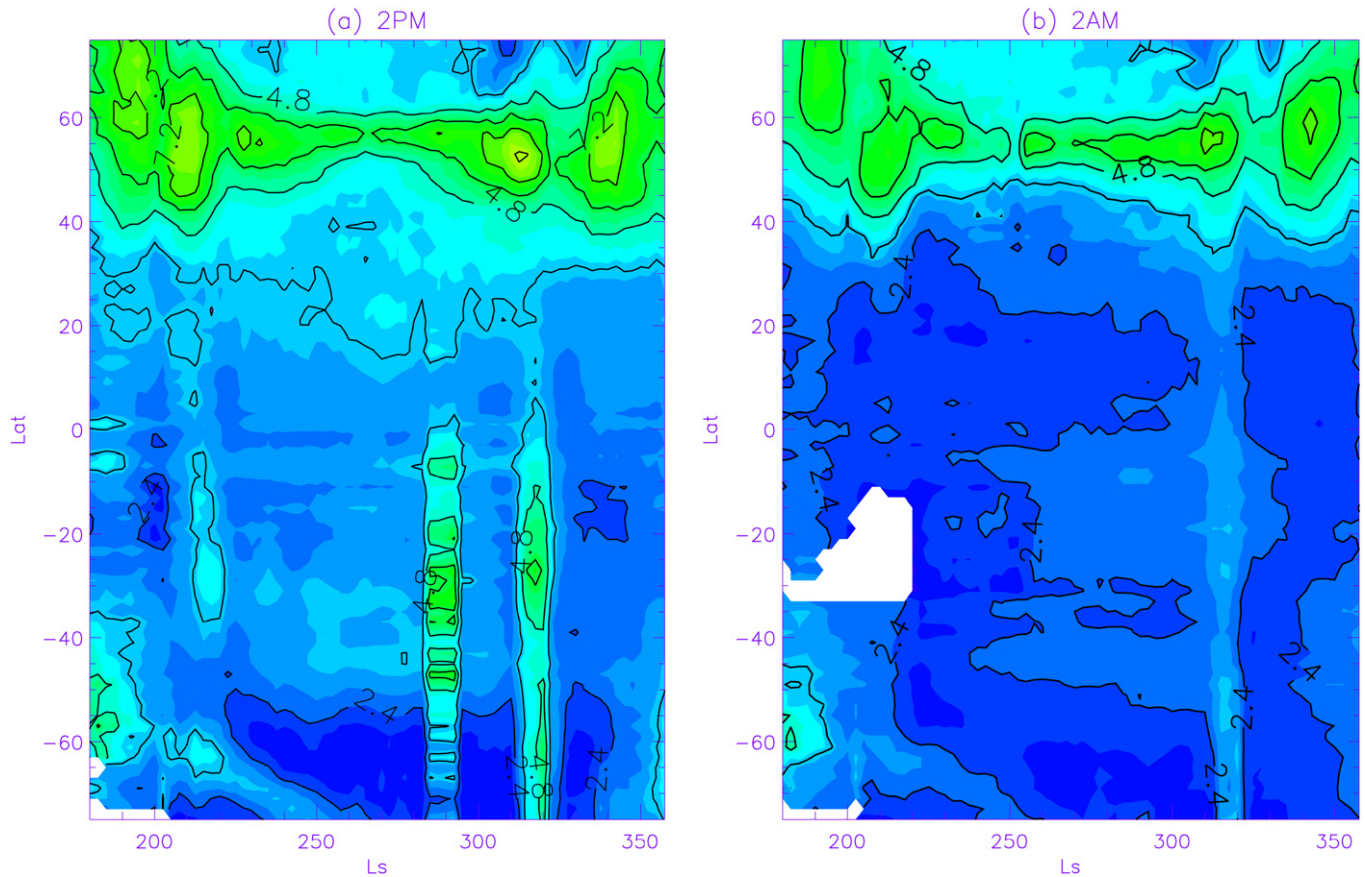


Fig. 7. The standard deviations of (a) 2PM (b) 2AM TES temperatures as a function of latitude and L_s for MY 26.

2PM standard deviations are about half those for L_s 310°–320°, signals for L_s 210°–220° may be too weak to show in the 2AM plot. The southern hemisphere shows an additional maximum in the 2PM standard deviations during 285°–295° that is stronger than the maximum for L_s 210°–220°. This maximum is also absent in the corresponding 2AM plot. Surprisingly, both the MDGM animations and the TES opacities show no significant dust storms or water ice clouds during L_s 285°–295°. Detailed examination of the 2PM TES temperatures for this period shows that they can swing from 60 K below to 20 K above the average at southern mid latitudes. The abnormal behavior of temperatures during this period is puzzling.

In the northern hemisphere, both the 2PM and 2AM plots in Fig. 7 point to the same pattern. Large standard deviations concentrate in a band between $\sim 45^\circ$ N and 65° N at the edge of the polar vortex. The band is the thinnest during $L_s \sim 250^\circ$ – 300° , $L_s \sim 220^\circ$ – 230° , and $L_s \sim 320^\circ$ – 330° . These three periods correspond nicely to the long gap and short gaps in the seasonal distribution of flushing dust storms described in Section 3. The standard deviations during the short gaps are smaller than those for the adjacent periods. The standard deviations during the long gap appear to have episodes of relatively large values in the 2AM plot. In agreement with the flushing dust storm observations, the strongest eddy activities indicated by the largest standard deviations and the largest areas of influence occur

during L_s 300°–320°, and the second strongest eddy activities occur during L_s 200°–220°. Substantial eddy activities return after $L_s \sim 330^\circ$ and $L_s \sim 230^\circ$, respectively.

The L_s –height distributions of the 2PM temperature standard deviations are shown in Fig. 8 for 48° N– 50° N, 54° N– 56° N, 58° N– 60° N, and 62° N– 64° N. The panels are meant to show the range of behaviors for the band of strong eddy activity at the polar vortex edge. For 48° N– 50° N (Fig. 8a), below ~ 10 km four large standard deviation periods corresponding to the four active flushing dust storm periods can be seen, consistent with Fig. 7. Above ~ 10 km, large standard deviations generally occur before L_s 220° and after L_s 310°, and the weak eddy activity region extends toward the surface around the northern winter solstice. The L_s 210°–220° and L_s 310°–320° periods, corresponding to the two strongest flushing dust storm periods, appear to have their upper level maxima vertically connected with the corresponding lower level maxima at ~ 10 km. In contrast, 62° N– 64° N (Fig. 8d) has stronger eddies above ~ 10 km than below ~ 10 km. There are additional maxima between the L_s 210°–220° and L_s 310°–320° maxima. Below ~ 10 km, strong eddies are present away from the northern winter solstice period, with temporary eddy suppression at $L_s \sim 205^\circ$ and 325° . Figs. 8b and 8c show the transition from prominent lower level activity of Fig. 8a to prominent upper level activity of Fig. 8d. In Fig. 8b, substantial eddy activities exist throughout the column during the northern winter solstice

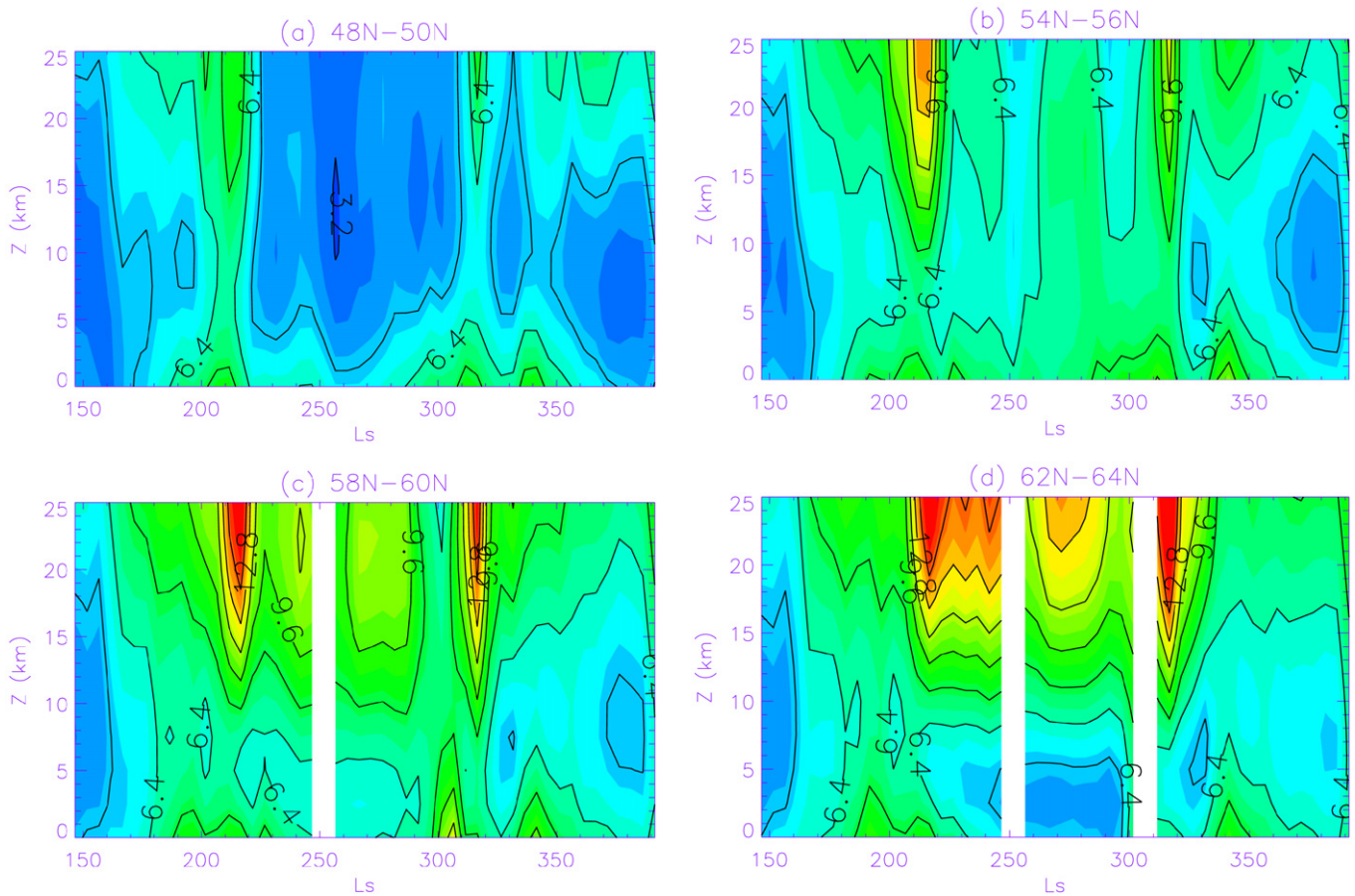


Fig. 8. L_s -altitude cross-sections of 2PM TES temperature standard deviations in MY 26 for selected latitudes. The latitudes are indicated above each panel.

period. The lower level maxima are weaker than the upper level ones, but are still discernable and correspond to the active flushing dust storm periods. In Fig. 8c, the upper level eddies become stronger and the lower level eddies become weaker than those in Fig. 8b during the northern winter solstice period.

The general features of Fig. 8 can be understood using Fig. 9, a latitude-height cross-section of the 2PM temperature standard deviations superimposed on the zonal mean temperatures for selected periods in MY 26. As expected, large standard deviations are concentrated in places where the temperature gradients are large (i.e., near the polar vortex edge). Isotherms at the edge of the polar vortex slope equatorward with height in the early fall. As the season progresses toward the northern winter solstice, they gradually change to slope in the opposite direction. During this process, the polar vortex shrinks in size and the temperature gradients sharpen. These changes are more dramatic at the upper levels than at the lower levels. After the winter solstice period, the polar vortex gradually changes back to slope equatorward with height and expands in size as the temperature gradients decrease with time. The anomaly during $L_s \sim 310^\circ\text{--}330^\circ$ in MY 26 associated with the Acidalia-Chryse dust-storm sequence highly perturbs the usual course of ‘recovery’: upper level mean temperatures at the northern high latitudes surge more than 20 K (also see Fig. 6) and upper level eddies dramatically increase in both amplitude and area of influence. The magnitude and location of eddy temperatures

closely follow the seasonal evolution of the polar vortex. Since the polar vortex shrinks to between 60°N and 70°N at upper levels and to between 50°N and 60° at lower levels during the northern winter solstice period, latitudes south of $\sim 55^\circ\text{N}$ lie outside the outer edge of the sharp temperature gradient band at upper levels but touch the band at lower levels, and latitudes north of $\sim 65^\circ\text{N}$ touch the band at upper levels but lie inside the inner edge of the band at lower levels. This explains why the standard deviations during the northern winter solstice period are smaller both at the upper levels in Fig. 8a and at the lower levels in Fig. 8d.

The change in the vertical temperature profiles from late summer/early fall to mid/late fall is also shown in Fig. 10 using MGS Radio Science (RS) data. RS temperature profiles have better vertical resolution than TES profiles, but they are limited in quantity. All RS profiles between 60°N and 80°N before the northern winter solstice in MY 26 are plotted for $L_s 160^\circ\text{--}210^\circ$ and $L_s 210^\circ\text{--}260^\circ$ in Fig. 10. The diamonds indicate the temperatures interpolated onto the pressure levels used by TES. The latitudes of these observations decrease from $\sim 80^\circ\text{N}$ to $\sim 60^\circ\text{N}$ and the local times gradually change from early afternoon ($\sim 1300\text{LT}$) to the morning ($\sim 0700\text{LT}$) during $L_s 160^\circ\text{--}260^\circ$. Differences in latitudes and local times can contribute some dispersion of the data, but the variations are largely due to the progress of the season. In agreement with the results from Fig. 9, late summer/early fall has large temperature vari-

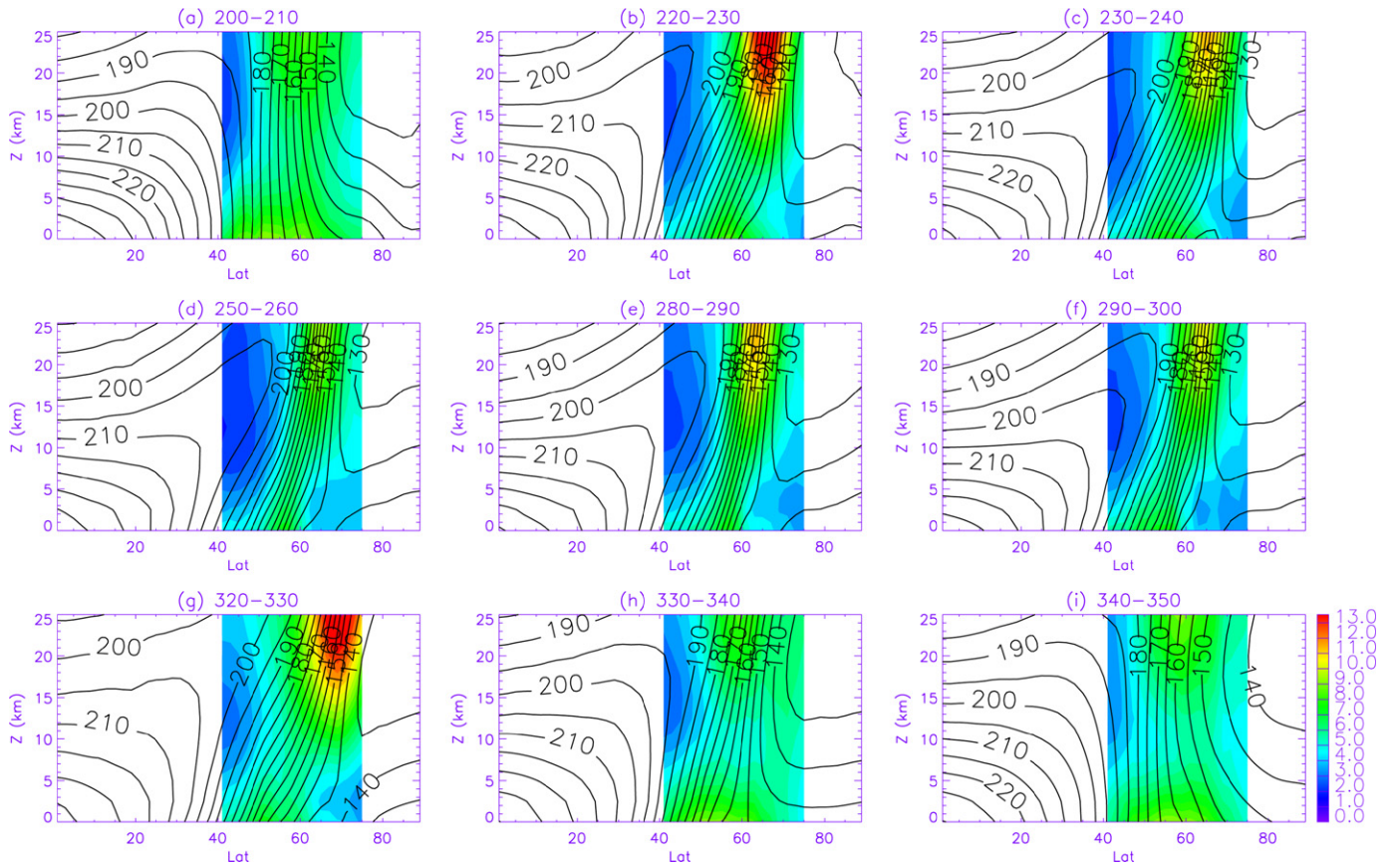


Fig. 9. Latitude–altitude cross-sections of 2PM temperature standard deviations superimposed on the corresponding zonal mean temperatures for selected periods in MY 26. The L_s ranges are labeled above the panels.

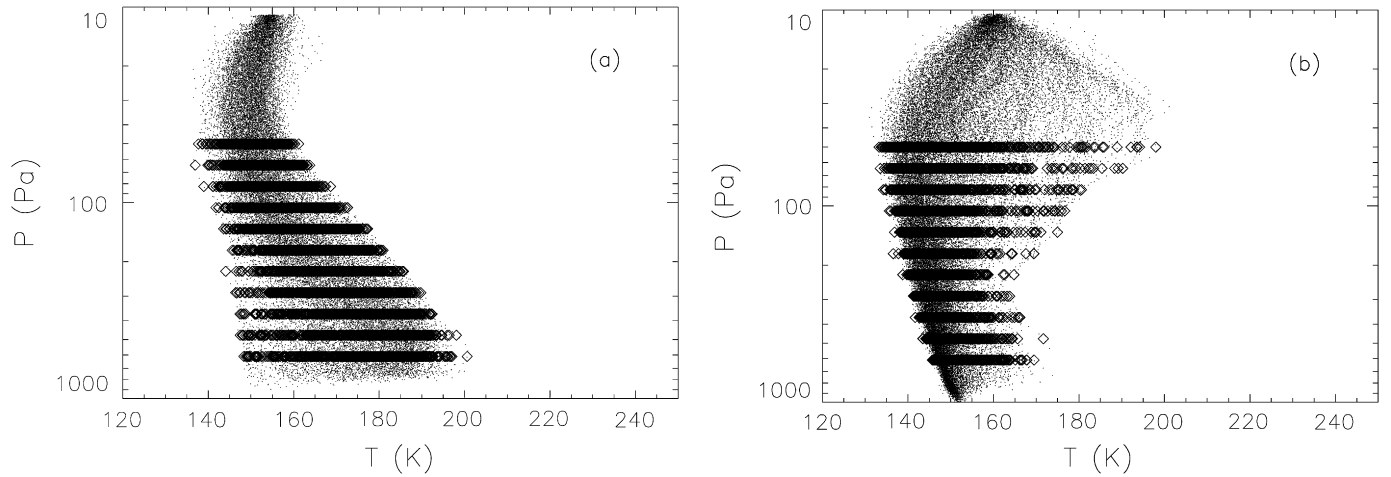


Fig. 10. Vertical temperature profiles derived by MGS Radio Science team for 60° N–80° N during (a) L_s 160°–210° and (b) 210°–260° of MY 26. The Diamonds indicate temperatures interpolated to the pressure levels used by the TES team.

ations at lower levels and mid/late fall has large variations at upper levels.

4.2.2. Waves

Banfield et al. (2003, 2004) studied the distributions of stationary, tidal, and traveling waves in great detail using MGS data obtained before MY 26. Their results show that traveling waves are the major component of eddies in the northern

mid and high latitudes, and that these waves follow the edge of the polar vortex, with wave number one mainly present at upper levels and wave number three at lower levels. Wang et al. (2005) showed that eddies at lower levels (especially wave number three) were better correlated with flushing dust storms for MY 24 and 25. The correlation between the lower-level eddies and the flushing dust storms for MY 26 has been demonstrated in Section 4.2.1. In agreement with previous studies,

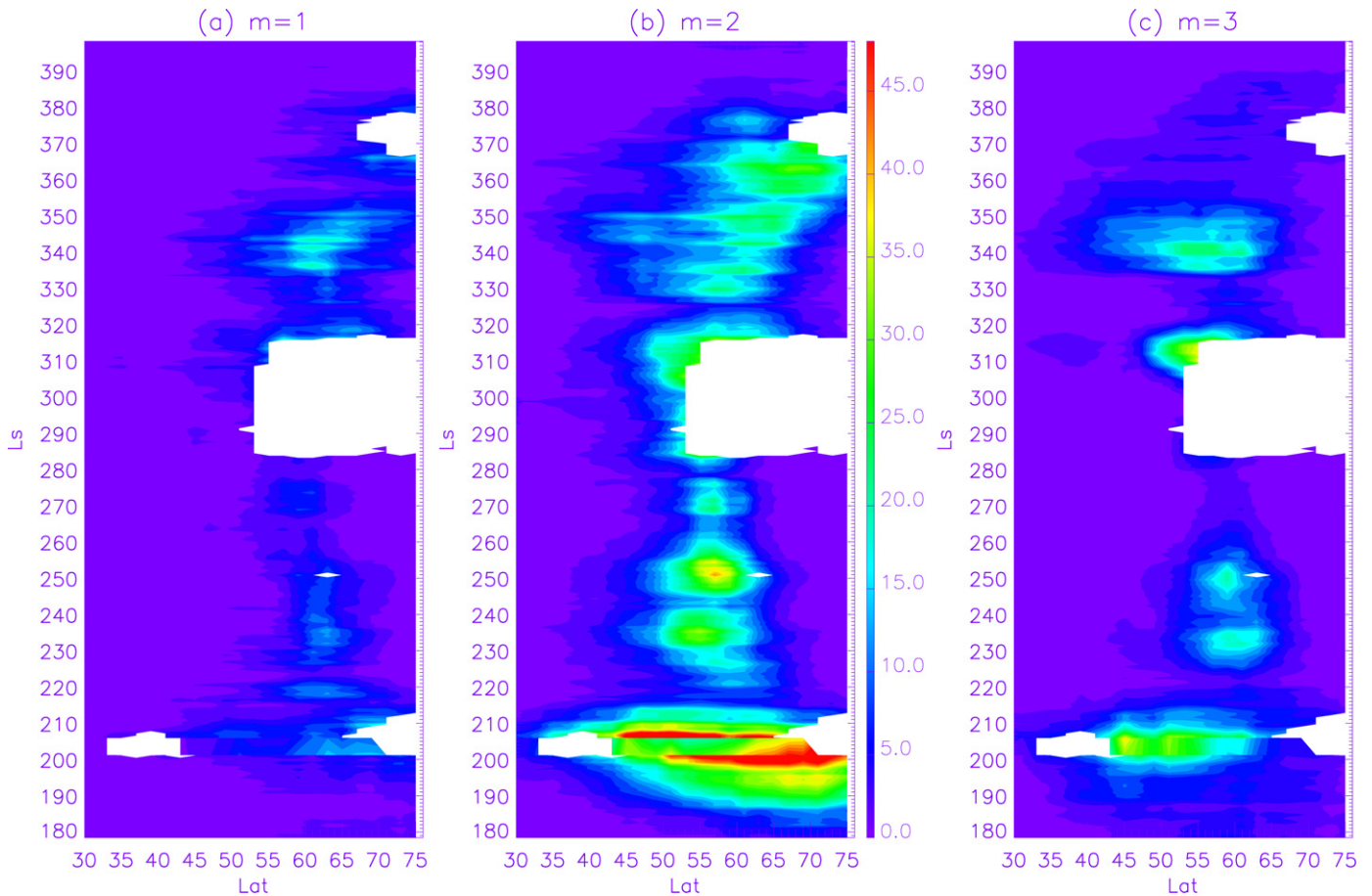


Fig. 11. Total power (K^2) of eastward traveling waves with periods between 2 and 4 days and zonal wavenumber (a) $m = 1$, (b) $m = 2$, (c) $m = 3$.

the correlation breaks down above the first scale height. Eddies at upper levels are active during the winter solstice periods. Among the wide range of wave modes exhibited at upper levels, the wave number $m = 1$ waves with periods longer than ~ 6 days are dominant. This paper will concentrate on the waves at lower levels.

Fig. 11 shows the power of the 2–4 sol eastward traveling wave $m = 1$, 2, and 3 at 4.75 mb as a function of latitude and L_s for MY 26. All waves show the general trend of weaker (in terms of either intensity or area of influence) activity around the northern winter solstice, but the most impressive correlation apparently comes from the $m = 3$ waves. Results from wave decomposition of the MGS RS data agrees with those from TES data (Hinson, 2006). The power of $m = 3$ waves is concentrated within four sub-periods (L_s 195°–215°, L_s 225°–255°, L_s 300°–320°, and L_s 335°–350°) that correspond nicely to the four active flushing dust storm sub-periods described in Section 3. Furthermore, the sub-periods with the largest power correspond nicely to the most vigorous flushing dust storm sequences. The $m = 3$ traveling waves have most of their power in the 2–3 sol range. The $m = 1$ and $m = 2$ waves have significant power in the 4–8 sol range in addition to the 2–4 sol range (not shown). The 4–8 sol $m = 1$ waves are mainly present during L_s 210°–225° and L_s 335°–350°, and the 4–8 sol $m = 2$ waves are mainly present during L_s 200°–215° and L_s 290°–300°.

Some periods with active $m = 1$ and $m = 2$ waves coincide with the active flushing dust storm periods while others do not. The $m = 1$ and $m = 2$ can combine with the 2–3 sol $m = 3$ waves to produce fronts that travel around the pole when they have the same phase speed (e.g., 6.7 sol $m = 1$, 3.3 sol $m = 2$ and 2.2 sol $m = 3$) (Banfield et al., 2004). Therefore, fronts are expected for at least two of the active flushing dust storm periods—the L_s 200°–220° and L_s 335°–350° periods. This is consistent with the presence of eastward traveling frontal dust storms in MDGM.

The concentration of flushing dust storms in Acidalia, Arcadia, and Utopia (Wang et al., 2005) suggests that they are more related to storm tracks than traveling fronts. Traveling waves with the same period can produce storm tracks (Banfield et al., 2004). Fig. 12 investigate how storms tracks from $m = 1$ –3 waves with the same periods correlate with flushing storms. Fig. 12a shows the total power of the 2.2-sol $m = 1$ –3 traveling waves. Large power mainly exists during L_s 230°–250° and L_s 300°–310°. These two periods coincide with two of the active flushing dust storm periods. Figs. 12b–12d show the individual power of the 2.2-sol $m = 1$, 2, and 3 wave, respectively. The $m = 3$ wave has a large contribution to the total power shown in Fig. 12a. However, 2.2-day $m = 1$ and 2 waves also have significant power during L_s 230°–250° and L_s 300°–310°. Therefore, eddies during these two periods are

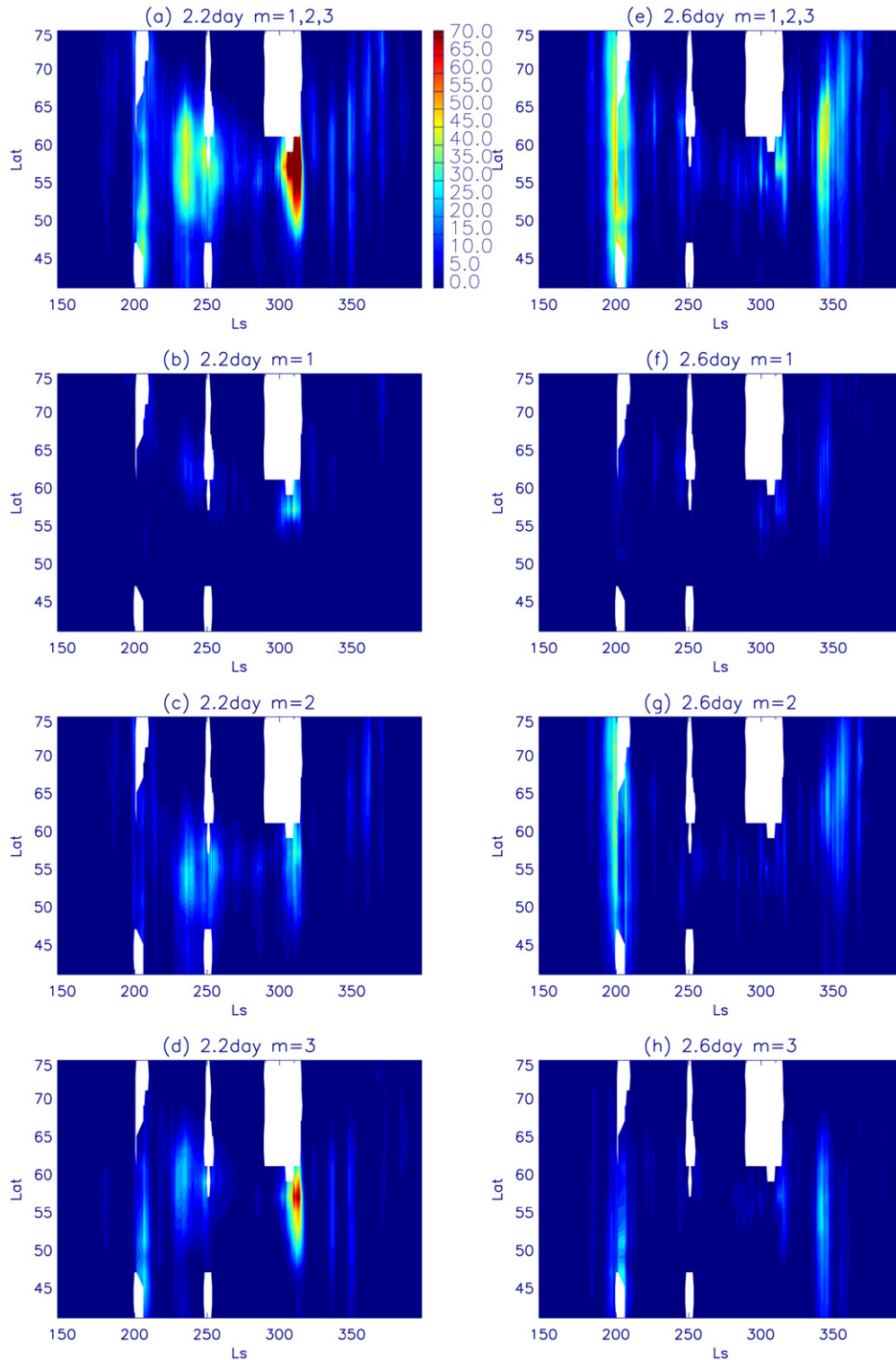


Fig. 12. (a) Total power (K^2) of eastward traveling 2.2-day $m = 1, 2$, and 3 waves. (b) Power of eastward traveling 2.2-day $m = 1$ wave. (c) Power of eastward traveling 2.2-day $m = 2$ wave. (d) Power of eastward traveling 2.2-day $m = 3$ wave. (e) Total power of eastward traveling 2.6-day $m = 1, 2$, and 3 waves. (f) Power of eastward traveling 2.6-day $m = 1$ wave. (g) Power of eastward traveling 2.6-day $m = 2$ wave. (h) Power of eastward traveling 2.6-day $m = 3$ wave.

expected to exhibit storm track behavior resulting from the 2.2-day traveling waves. Fig. 12e shows the total power of the 2.6-sol $m = 1-3$ waves. Large power mainly exists during $L_s 200^\circ-210^\circ$ and $L_s 340^\circ-350^\circ$ which lie within the other two active flushing storm periods. Figs. 12f–12h show the power

of 2.6-sol $m = 1, 2$, and 3 waves, respectively. In this case, both the $m = 3$ and $m = 2$ waves have significant contributions to the total power shown in Fig. 12e, indicating storm tracks during these periods. In summary, Fig. 12 shows that different flushing dust storm periods are associated with storm

tracks made from different wave modes (e.g., 2.2-day waves or 2.6-day waves). Furthermore, results in the previous paragraph and this paragraph combined show that storm tracks can coexist with fronts during certain flushing dust storm periods.

5. Summary

The distribution of flushing dust storms in the third MGS mapping year (MY 26, 2003–2005) is presented in this paper. In agreement with the results for the previous two Mars years, flushing dust storms are especially active before and after a quiet period near the northern winter solstice during which there are no such storms. A special feature of MY 26 is that a statistically significant short gap in the seasonal distribution is observed in the pre- and post-solstice periods. The L_s 300°–320° and L_s 200°–220° sub-periods in MY 26 are the most active ones. Flushing dust storm sequences lead to dust accumulation in the southern hemisphere, resulting in significant perturbation to the large-scale structure of the atmosphere. The effects of these major dust storms on the atmosphere are represented best by different fields at different altitudes. At upper levels, the perturbed zonal mean temperatures as a function of latitude and L_s show prominent dumbbell shapes with warmer temperatures at the northern and southern mid and high latitudes indicating an enhanced Hadley circulation due to increased dust loading. However, traveling waves at upper levels ($m = 1$ and 2) are generally stronger during the northern winter solstice period, which is opposite to the observed behavior of frontal dust storms. At lower levels, the signatures of the major dust storms are not easily recognizable in the zonal mean temperatures. However, the eastward $m = 3$ traveling waves with periods between 2 and 3 days coincide with active frontal and flushing dust storms. The $m = 3$ waves combine with other waves of the same periods to make storm tracks during each active sub-period. Sometimes, they also combine with other waves of the same phase speed to make fronts.

6. Discussion

The $m = 1$ and 2 waves have deep vertical structures and are dominated by periods longer than 4 sols (Banfield et al., 2004). Modeling studies confirm that deeper structures are observed at longer wavelengths (Barnes et al., 1993; Wilson et al., 2002; Newman et al., 2002). Wilson et al. (2002) show that the $m = 1$ wave is dominated by a period of 6.7 sol and can have significantly longer period at higher altitudes. The $m = 3$ waves are confined near the ground, have periods between 2 to 3 sols, and mainly occur away from the northern winter solstice. Hourdin et al. (1995) found a tendency for increased suppression of traveling wave activity during northern hemisphere winter solstice season as dust loading is increased in the LMD Mars GCM. Basu et al. (2006) simulated the transition between short and long period traveling waves using the GFDL Mars GCM.

Multiple short active flushing dust storm sub-periods within the long pre- or post-solstice periods were conjectured by Wang et al. (2005) based on previous Viking and MGS observations.

They reasoned that major dust storms early in the long active period could, through the intensification of the Hadley circulation, temporarily set the atmosphere into a state closer to that typical of the northern winter solstice (Wang et al., 2005). This would briefly halt the formation of frontal and flushing dust storms. This is the first time that such sub-periods are clearly identified. The response of the atmosphere to the major dust storms in MY 26 shows clear signatures of an enhanced Hadley circulation. The effects of the L_s 200°–220° sequence last for $\sim 10^\circ L_s$ which is short enough for the return of flushing dust storms before the long winter solstice gap. The L_s 300°–320° sequence involves more dust and produces stronger atmospheric perturbations (e.g., polar warming), but its effects last for only $\sim 10^\circ L_s$ as well, probably because the season is departing from the winter solstice. Flushing dust storms return after the hiatus and gradually move north with the band of strong eddies at the edge of the polar vortex. This is another example in support of the idea that the time of formation of major dust storms affects the duration and degree of their impact.

Throughout the northern fall and winter, the latitudinal band around the edge of the north polar vortex shows stronger eddies than other latitudes. The vertical distribution of eddy temperature shows an upper level and a lower level maximum (Fig. 9), a feature simulated by the NASA AMES Mars GCM (Barnes et al., 1993). The upper level eddies are dominated by wave number $m = 1$ and $m = 2$. The lower level eddies are dominated by wave number $m = 2$ and $m = 3$. The altitude with the minimum eddy temperature within the band varies between ~ 5 and ~ 15 km and depends on the strength of the upper level eddies: stronger upper level eddies (e.g., during the winter solstice period or major dust storms) lead to a lower height. With the strengthening of the temperature gradients at the polar vortex edge, the wind contours of the jet descend in altitude as well (Banfield et al., 2003). The movement of the altitude of the weakest eddy temperature location appears to follow that of the 20 m/s contour, which is approximately the phase speed of the 2–3 sol wave number $m = 3$ wave, the 3–4 sol wave number $m = 2$ wave, and the 6–7 sol wave number $m = 1$ wave. Wilson et al. (2002) comment on the eddy structure and its association with a “steering level” at the level of the 20 m/s zonal wind contour.

The three mapping years of MGS observations show a variety of paths for the development of major dust storms. The MY 24 and MY 26 dust storm sequences are triggered by flushing dust storms that transport dust from the northern to the southern hemisphere through the Acidalia–Chryse or Utopia channel. The MY 25 global dust storms are triggered by dust storms locally generated in or around Hellas basin. The subsequent development of these major events was examined by data assimilation using the AOPP/LMD MGCM (Montabone et al., 2005). Merging of dust storms (Cantor et al., 2001) occurred in all three Mars years. The observed number of mergings during the seasons examined is 12, 4, and 3 for years 1, 2, and 3, respectively, although the actual number could be larger because the MDGM only examine the early afternoon hours (~ 2 PM). The difference between the first and the other two Mars years could be real; however, it is possible that the major-

ity of merging events in different years occur at a different local time, which could make MGS mapping Year 1 appear to have more merging events. Newman et al. (2002) simulated Chryse- and Hellas-type dust storms with radiatively active dust transport and parameterized dust lifting in the AOPP/LMD MGCM. Their results showed that positive feedbacks between the atmospheric state and threshold sensitive stress lifting could trigger further dust lifting once the initial dust storm formed. This is consistent with the observations that major dust storms are associated with dust storm sequences that exhibit multiple centers of activity, with later dust lifting enhancing earlier lifting. Basu et al. (2006) also simulated Chryse- and Hella-type dust storms with the GFDL MGCM. In agreement with observations, they showed that the simulated transient waves are weaker during the northern winter solstice period. They also state that the Chryse-type dust storms are larger at lower obliquities and can grow into global dust storms.

During the aerobraking and science phase of MGS (MY 23), TES observed two regional dust storms in the southern hemisphere. One occurred in Noachis during L_s 225°–233° and the other occurred north of Argyre at $L_s \sim 309^\circ$ (Smith et al., 2000). The time of occurrence is well within the active flushing dust storm periods. Based on the experience from MY 26, the locations are also within the reach of flushing dust storm sequences. Although the MY 23 regional dust storms are very likely to be locally generated, there is a possibility that they could be related to flushing dust storms. Unfortunately, no global maps were taken at the time to clarify the development histories of these dust storms.

MGS observations show that the enhancement of the Hadley circulation is accompanied by the suppression of lower level transient eddies (associated with frontal dust storms) and the amplification of upper level transient eddies at northern mid and high latitudes, suggesting that energy is re-partitioned between different circulation components. Using Viking data, Leovy et al. (1985) noticed that the circulation of the global dust storm years was characterized by an enhanced Hadley circulation and suppressed baroclinic waves. Haberle (1986) attempted to explain the interannual variability of global dust storms based on the idea that northern baroclinic waves would increase dust in the northern hemisphere which would suppress the Hadley circulation and global dust storms. While the anti-correlation between the Hadley circulation and lower level baroclinic eddies is still true, dust initially raised in northern frontal dust storms can apparently travel to the southern hemisphere and lead to substantial enhancement of the Hadley circulation. Transient eddies at northern mid and high latitudes are studied in this paper because they are directly relevant to the frontal dust storms observed in images. Other circulation components, such as the thermal tides and stationary waves, certainly change with season and dust as well (Banfield et al., 2000, 2003; Lewis and Barker, 2005; Wilson and Richardson, 2000), but these topics are beyond the scope of this paper.

Acknowledgments

The author would like to thank Phil James and an anonymous reviewer for reviews, John Wilson and Chris Walker for comments. This research project is supported by funding from Harvard University.

References

- Banfield, D., Conrath, B.J., Pearl, J.C., Smith, M.D., Christensen, P.R., 2000. Thermal tides and stationary waves on Mars as revealed by Mars Global Surveyor thermal emission spectrometer. *J. Geophys. Res.* 105, 9521–9537.
- Banfield, D., Conrath, B.J., Smith, M.D., Christensen, P.R., Wilson, R.J., 2003. Forced waves in the martian atmosphere from MGS TES nadir data. *Icarus* 161, 319–345.
- Banfield, D., Conrath, B.J., Gierasch, P.J., Wilson, R.J., Smith, M.D., 2004. Traveling waves in the martian atmosphere from MGS TES nadir data. *Icarus* 170, 365–403.
- Barnes, J.R., 1980. Time spectral analysis of midlatitude disturbances in the martian atmosphere. *J. Atmos. Sci.* 37, 2002–2015.
- Barnes, J.R., Pollack, J.B., Haberle, R.M., Leovy, C.B., Zurek, R.W., Lee, H., Schaeffer, J., 1993. Mars atmospheric dynamics as simulated by the NASA Ames general circulation model. 2. Transient baroclinic eddies. *J. Geophys. Res.* 98, 3125–3148.
- Basu, S., Wilson, R.J., Richardson, R.I., Ingersoll, A.P., 2006. Simulation of spontaneous and variable global dust storms with the GFDL Mars GCM. *J. Geophys. Res.* 111, doi:10.1029/2005JE002660. E09004.
- Cantor, B.A., James, P.B., Caplinger, M., Wolff, M.J., 2001. Martian dust storms: 1999 Mars Orbiter Camera observations. *J. Geophys. Res.* 106, 23653–23687.
- Haberle, R.M., 1986. Interannual variability of global dust storms on Mars. *Science* 234, 459–461.
- Haberle, R.M., Pollack, J.B., Barnes, J.R., Zurek, R.W., Leovy, C.B., Murphy, J.R., Lee, H., Schaeffer, J., 1993. Mars atmospheric dynamics as simulated by the NASA AMES general circulation model. 1. The zonal–mean circulation. *J. Geophys. Res.* 98, 3093–3123.
- Hinson, D.P., 2006. Radio occultation measurements of transient eddies in the northern hemisphere of Mars. *J. Geophys. Res.* 111, doi:10.1029/2005JE0026512. E05002.
- Hourdin, F., Forget, F., Talagrand, O., 1995. The sensitivity of the martian surface pressure and atmospheric mass budget to various parameters: A comparison between numerical simulations and Viking observations. *J. Geophys. Res.* 100, 5501–5523.
- Jakosky, B.M., Martin, T.Z., 1987. Mars: North-polar atmospheric temperatures during dust storms. *Icarus* 72, 528–534.
- Lewis, S.R., Barker, P.R., 2005. Atmospheric tides in a Mars general circulation model with data assimilation. *Adv. Space Res.* 36, 2162–2168.
- Leovy, C.B., Tillman, J.E., Guest, W.R., Barnes, J.R., 1985. In: Hunt, G.E. (Ed.), *Recent Advances in Planetary Meteorology*. Cambridge Univ. Press, Cambridge, pp. 69–84.
- Liu, J., Richardson, M.I., Wilson, R.J., 2003. An assessment of the global, seasonal, and interannual spacecraft record of martian climate in the thermal infrared. *J. Geophys. Res.* 108, doi:10.1029/2002JE001921.
- Montabone, L., Lewis, S.R., Read, P.L., 2005. Interannual variability of martian dust storms in assimilation of several years of Mars global surveyor observations. *Adv. Space Res.* 36, 2146–2155.
- Newman, C.E., Lewis, S.R., Read, P.L., Forget, F., 2002. Modeling the martian dust cycle. 2. Multi-annual radiatively active dust transport simulations. *J. Geophys. Res.* 107, doi:10.1029/2002JE001920.
- Smith, M.D., 2004. Interannual variability in TES atmospheric observations of Mars during 1999–2003. *Icarus* 167, 148–165.
- Smith, M.D., Pearl, J.C., Conrath, B.J., Christensen, P.R., 2000. Mars Global Surveyor Thermal Emission Spectrometer (TES) observations of dust opacity during aerobraking and science phasing. *J. Geophys. Res.* 105, 9539–9552.

- Smith, M.D., Conrath, B.J., Pearl, J.C., Christensen, P.R., 2002. Thermal emission spectrometer observations of martian planet-encircling dust storm 2001A. *Icarus* 157, 259–263.
- Strausberg, M.J., Wang, H., Richardson, M.I., Ewald, S.P., Toigo, A.D., 2005. Observations of the initiation and evolution of the 2001 Mars global dust storm. *J. Geophys. Res.* 110, doi:10.1029/2004JE002361.
- Wang, H., Ingersoll, A.P., 2002. Martian clouds observed by Mars Global Surveyor Mars Orbiter Camera. *J. Geophys. Res.* 107, doi:10.1029/2001JE001815.
- Wang, H., Richardson, M.I., Wilson, R.J., Ingersoll, A.P., Toigo, A.D., Zurek, R.W., 2003. Cyclones, tides, and the origin of a cross-equatorial dust storm on Mars. *Geophys. Res. Lett.* 30, doi:10.1029/2002GL016828.
- Wang, H., Zurek, R.W., Richardson, M.I., 2005. Relationship between frontal dust storms and transient eddy activity in the northern hemisphere of Mars as observed by Mars Global Surveyor. *J. Geophys. Res.* 110, doi:10.1029/2005JE002423.
- Wilson, R.J., 1997. A general circulation model simulation of the martian polar warming. *Geophys. Res. Lett.* 24, 123–126.
- Wilson, R.J., Richardson, M.I., 2000. The martian atmosphere during the Viking mission, I. Infrared measurements of atmospheric temperature revised. *Icarus* 145, 555–579.
- Wilson, R.J., Banfield, D., Conrath, B.J., Smith, M.D., 2002. Traveling waves in the northern hemisphere of Mars. *Geophys. Res. Lett.* 29, doi:10.1029/2002GL014866.